MADRID
inter.noise 2019
June 16 - 19
NOISE CONTROL FOR A BETTER ENVIRONMENT

Use OpenFOAM coupled with Finite and Boundary Element Formulations for Computational Aero-Acoustics for Ducted Obstacles

De Reboul, Silouane[1]
ESI Group, CoE Vibro-Acoustics
8, Rue Clement Bayard, 60200 Compiegne, France

Zerbib, Nicolas[1]
ESI Group, CoE Vibro-Acoustics
39, Chemin des Ramassiers, 31170 Colomiers, France

Heather, Andrew[3]
OpenCFD
Unit 6 The Courtyard Eastern Road, Bracknell, Berkshire RG12 2XB, UK

ABSTRACT

In the coming years, more hybrid and full electric vehicles will be coming to the market and some new challenges will arise for noise and vibration engineers. One of them is the flow induced noise within ducts and vents in HVAC systems leading potentially to customer complains. Several numerical approaches are possible to simulate this problem. First, using a compressible form of equation of state for the fluid, the hydrodynamic source mechanisms and the sound propagation in a compressible liquid domain can be computed directly. In parallel, hybrid methods can also be applied assuming the decoupling of noise generation and propagation. First, an incompressible turbulent flow field is performed delivering aeroacoustic equivalent sources. Secondly, several Acoutic Analogies Finite or Boundary Element formulations are solved in the Fourier space. To save some CPU time and some space disk, the aero-acoustic source terms are transferred from the fluid mesh to the acoustic mesh by a conservative algorithm to guaranty the quality of the aeroacoustic phenomena on the fly, i.e. at the end of each time step during the CFD computation. This approach appears to be very suitable for industrial applications and is applied to a 3D ducted diaphragm with a low Mach number flow. The numerical results are compared between the Curle's BEM analogy for which only the dipole sources are taken into account through a Fluctuating Surface Pressure representation, both FEM Ribner and Lighthill analogies with volume field source representations and experimental measurements. Even if very good agreements are found in terms of flow dynamic and acoustic results with all the methods compared with measurements (PIV for the flow and downstream microphone for the acoustic), the FEM Ribner or Lighthill's acoustic analogies are revealed to be the best candidate for industrial applications using less computational resources and a full 3D description of the aero-acoustic sources.

Keywords: Computational Aeroacoustic Analogies, Ducted Obstacles, Finite/Boundary Element Methods
I-INCE Classification of Subject Number: 11

1. INTRODUCTION

In many practical applications, sound is generated by the interaction of turbulent flow with solid walls. In this situation, the acoustic wave experiences multiple reflections before propagation to a far field. Therefore, the sound spectrum exhibits rich frequencies content consisting of broadband and tonal components. To predict the acoustics field in these situations, a general aero-acoustic framework is required. More importantly, the employed method must often avoid many simplifying assumptions about geometry, compactness, or frequency content of sound sources. The prediction of flow-induced noise requires accounting for the physics of both unsteady flow and the sound wave, simultaneously, since both are a solution of the compressible Navier-Stokes equation. The basic difficulties for such computations are numerous disparities between energies and length scale in the turbulent flow and the sound field. Sound waves carry only a minuscule fraction of the flow energy, and a high order numerical scheme is required to keep the sound wave intact. These fundamental differences are exacerbated in a low Mach number flow [1] where the radiated acoustic power is smaller than the hydrodynamic flow power by roughly $\boldsymbol{O}(\boldsymbol{M^4})$. In addition, the acoustic CFL number imposes extremely small time steps on the numerical solution in order to resolve both acoustics and hydrodynamics. That is why it is commonly accepted that hybrid methods are more appropriate for low Mach number flows. An example of a two-step or hybrid method for nearly incompressible flows is Lighthill [2] who formally separated acoustics from hydrodynamics by introducing his acoustic analogy. It was shown that the flow mechanism that produced noise could be expressed in the form of equivalent sources in a uniform medium at rest, chosen as a representation of the propagation region surrounding the listener. The idea of equivalent sources has proven to be quite powerful at low Mach numbers. Curle [3] extended the Lighthill analogy to predict the sound of turbulent-body interaction by introducing a dipole source. Ffowcs Williams and Hawkings [4] generalized previous analogies to account for moving sources, impermeable rigid surfaces and the resulting Doppler effects.

Most of the works in the literature are dedicated for exterior problems. In the present work, we are concerned with the noise generated by confined flows and its propagation within the duct. The interaction of pipe flow with singularities such as diaphragm, valve contractions, or pipe junctions are sources of internal noise in industrial duct networks [5-6]. The problem of aerodynamics sound generation in pipes, allowing the aeroacoustics analogy by Davies and Ffowcs Williams [7] showed that the acoustic efficiency of turbulence within a straight infinite duct varies with frequency from a dipole-like behavior below the cut-off frequency to free-field quadrupole efficiency as soon as a few transverse modes are cut-on. Nelson and Morfey [8] Peters and Hirschberg [9] and Piellard [10] have focused on the prediction of noise generated by duct geometrical discontinuities. Low frequencies are often considered [11] which has two advantages: firstly, the source is acoustically compact; secondly, for frequencies below the duct cut-off, the one-dimensional Green's function can be employed. However, in many engineering products that contain ducts, the spectrum of interest often extends beyond the transverse cut-off frequency, up to several KHz. Mak [12] and Han and Mak [13] formulated the sound powers produced by the interaction of multiple in-duct

elements at frequencies below and above the first transverse duct mode cut-on frequency. The general scope of this work is to develop, validate and compare some acoustic FEM formulations to deal with the configuration corresponding to experiments of Bennouna et al. [14] and the DES/BEM numerical result of Escouflaire and al. [15] exploiting only the hydrodynamic pressure or the Lighthill tensor volume fields as CFD data.

In general, the hybrid approach of flow noise computation based on aero-acoustic analogies is a prediction method which is well suited for low Mach number flows in view of the strong disparities between the properties of hydrodynamic fluctuations and those of resulting acoustic waves. The generated noise due to turbulent flow is estimated in three steps as illustrated Fig. 1.

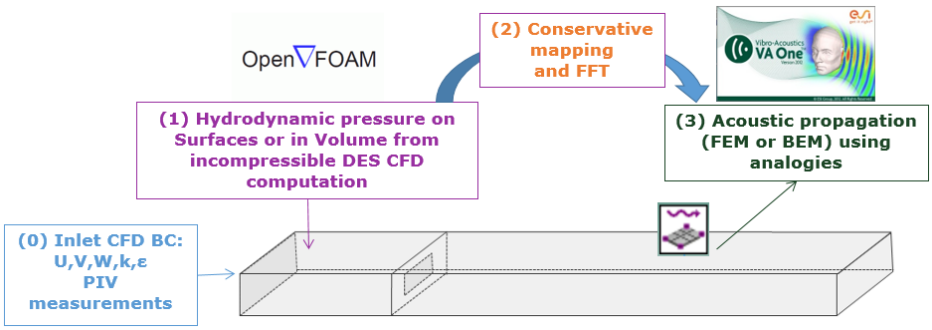

Figure 1: Aeroacoustics procedure to simulate the noise radiated inside a duct (example based on the single diaphragm case).

First, an incompressible Detached Eddy Simulation (DES) of the turbulent flow is performed, during which aero-adynamic quantities are recorded on the acoustic mesh after an on-the-fly volume conservative mapping between both meshes. In a second step, aero-acoustic analogies are solved by the Lighthill's [2] or Ribner [29] equations using a variational approach [1]. This paper is organized as follows: first of all, the DES flow model done with OpenFOAM is presented, then a derivation of the BEM variant of Curle's analogy to predict the aeroacoustics is given [16], following by the standard Lighthill's analogy and a derivation of the FEM variant of Lighthill's analogy with the pressure correction called Ribner's analogy as it has been done for the BEM variant of Curle's analogy [17]. Finally, we demonstrate the applicability of three methods to engineering problems by computing the sound of internal confined flow through a ducted diaphragm underlying the positive point of the FEM approaches compared with the BEM one.

[1] nicolas.zerbib@esi-goup.com, web page: http://www.esi-group.com
[2] a.heather@opencfd.co.uk, web page: http://www.openfoam.com

2. FLOW MODEL

2.1 Delayed Detached Eddy Simulation

Large Eddy Simulation (LES) is promising to overcome the disadvantages of the Reynolds-Averaged Navier Stokes (RANS) model. In LES, the governing equations are spatially filtered on the scale of the numerical grid. The large energy containing scales are directly simulated, and the small scale eddies, which are generally more homogeneous and universal, are

modeled. The large eddies are strongly affected by the flow field geometry boundaries. Therefore, the direct computation of the large eddies by LES is more accurate than the modeling of the large eddies by RANS. However, to resolve the wall boundary layer, LES needs the CPU resource not much less than the Direct Numerical Simulation (DNS). For engineering applications, it is not hopeful for LES to be rigorously used until in another 4 decades [18].

To overcome the intensive CPU requirement for LES, Spalart et al. [18] developed the detached eddy simulation (DES) strategy, which is a hybrid RANS and LES method. Near the solid surface within the wall boundary layer, the unsteady RANS model is realized. Away from the wall surface, the model automatically converts to LES. By using the RANS model near walls, the mesh size as well as the CPU time can be tremendously reduced. The motivation of DES is that the LES is powerful in regions of massive separation and other free shear flows such as jets, but much too costly in the large area of thin wall boundary layers.

However, a defect of the first generation DES model [18], has been also exposed. DES model in reference [18] may behave incorrectly in the regions of thick boundary layers and shallow separation regions due to the grid spacing dependence [19]. Delayed detached-eddy simulation (DDES) by Spalart [19] is an improved version of the original DES model [18]. With DDES, a blending function similar to the one used by Menter and Kuntz [20] for the shear stress transport (SST) model is introduced to limit the length scale of [18] to ensure the transition of RANS to LES be independent of grid spacing. Spalart et al. [19] validated DDES for a flat plate with the wall-parallel grid spacing about 1/10th of the boundary layer thickness (severe grid or ambiguous grid defined by Spalart). This DDES is the hybrid RANS/LES turbulent formulation used to simulate the CFD computation to save some CPU time with a good enough accuracy for engineering instead of the standard RANS or LES.

2.2 Mesh

The application case is ducted diaphragm of $\mathbf{1.904}\ \boldsymbol{m}$ length whose rectangular cross-section is $\mathbf{20}\ \boldsymbol{cm} \times \mathbf{10}\ \boldsymbol{cm}$, which presents a constriction of $\mathbf{10}\ \boldsymbol{cm} \times \mathbf{5}\ \boldsymbol{cm}$ and thickness $\mathbf{8}\ \boldsymbol{mm}$ located at $\boldsymbol{z} = \mathbf{0.296}\ \boldsymbol{m}$. The mesh is composed by $\mathbf{5.2}$ million hexahedral cells. Three successive refinement zones are created around the diaphragm as can be seen in Fig. 2. The first one (level 1 of refinement) is set between $\boldsymbol{z} = \mathbf{0.26}\ \boldsymbol{m}$ and $\boldsymbol{z} = \mathbf{0.48}\ \boldsymbol{m}$, the second (level 2) between $\boldsymbol{z} = \mathbf{0.28}\ \boldsymbol{m}$ and $\boldsymbol{z} = \mathbf{0.36}\ \boldsymbol{m}$. Finally, the third (level 3) smallest one is set around the diaphragm. Between each level of refinement, the cell size is divided by two.

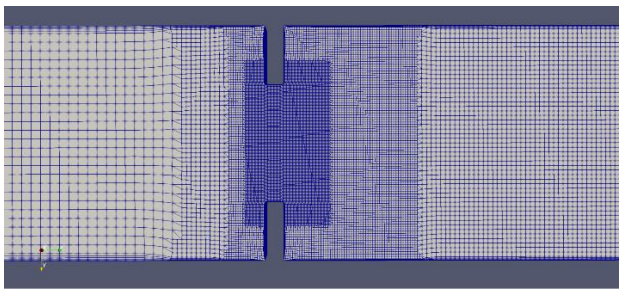

Figure 2. The 3 zones of mesh refinement around the diaphragm

Mesh Type	Hexahedron
Base cell length (level 0 of refinement)	4 mm
Diaphragm cell length (level 3)	0.5 mm
Number of boundary layers	5
Boundary layers thickness	0.8 mm
Total number of cells	5.2 M

Table 1. Parameters of the in-duct diaphragm mesh for the DDES.

Principal parameters of the mesh are summed up in the Table 1 and the parameters of the DDES on OpenFOAM are given in the Table 2. A parametric study has shown the importance of the tight refined mesh around the diaphragm (level 3 of refinement) to ensure a sufficiently accurate estimation of the acoustic sources in this area. On the other side, an extension of level 1 of refinement downstream of the diaphragm has little impact on the acoustic solution. A 5-level boundary layer is set on all faces of the duct and diaphragm.

Turbulence Model	Spalart-Allmaras DDES (see ref [19])
Simulated Physical Duration	0.057 sec
Time step	2.10-5 (record every time step)
Computation Time	5 hours
Computation Ressources	16 CPUs

Table 2. Parameters of the DDES on OpenFOAM®

2.3 Initial and Boundary Conditions

The duct inlet conditions are based on the values of velocity $(\boldsymbol{u}, \boldsymbol{v}, \boldsymbol{w})$ and the turbulent kinetic energy $\boldsymbol{k}$ obtained by PIV measurements interpolated on the DDES mesh as illustrated in Fig. 3. The value of the turbulent dissipation $\boldsymbol{\varepsilon}$ is set uniformly on the duct inlet face to the value of $\boldsymbol{\varepsilon = 0.24\, J/(kg.s)}$. The outlet condition consists, for its part, of a standard static pressure condition (where pressure is set to the atmospheric value). The mean value of the flow velocity on the 3D duct is equal to $\boldsymbol{6.4\, m/s}$.

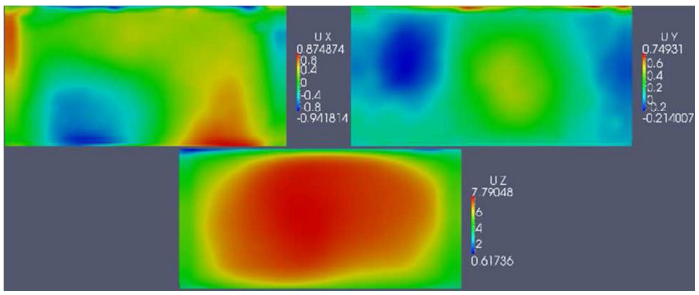

Figure 3. Interpolation of inlet PIV velocity data (u, v, w) on the CFD mesh

2.4 Simulation Parameters

The turbulence model is based on an improvement of the Spalart-Allmaras model that ensures a resistance to ambiguous grid densities, also referred to as Delayed Detached Eddy Simulation (DDES). Although the mesh previously described is a priori not ambiguous in the present case, this formulation was nevertheless chosen for its simplicity and adaptability to a diverse range of cases [16]. The DES is performed on a physical duration time of $\boldsymbol{0.057\ secs}$ on the single diaphragm case getting rid of a potential delay of the turbulence mechanisms, as can be observed with that class of methods. The case presented here is carried out in parallel on $\boldsymbol{16}$ CPU cores, on a Sandy Bridge Linux machine Intel Xeon E5-2680 2.7 GHz.

2.5 Simulation Parameters

So as to be compared qualitatively to the experimental data, the results of the simulation are plotted in terms of velocity field (in m/s) near the constriction on a longitudinal slice located at $\boldsymbol{x = 92\ mm}$ and on transversal slices located at $\boldsymbol{z = -100\ mm}$ and $\boldsymbol{z = +30\ mm}$ from the center of the diaphragm (see Fig. 4). The values of the velocity field are averaged at each time step by OpenFOAM.

These results can be qualitatively compared to the experimental and numerical results of papers [15,17,21]. In the latter, a LES simulation has been performed on the same case. A very

good agreement is observed with the experimental data. The DES predictions were unable to resolve the recirculation zones downstream the vena contracta but the averaged value calculated in those zones appears accurate enough not to affect the acoustic calculations (as will be seen in the following).

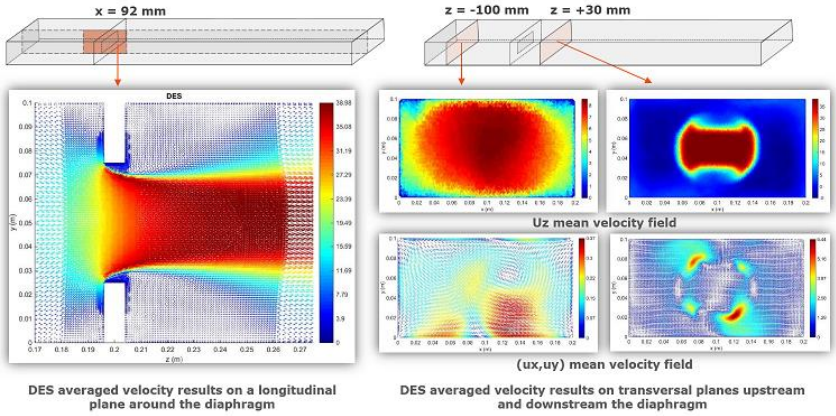

Figure 4. Visualization of the velocity field near the diaphragm on a slice at x = 92 mm (in m/s). The velocity field is not averaged on the entire DES time calculation.

At that stage, the equivalent aero-acoustic sources are computed thanks to the incompressible DDES CFD model described above and it is now a question of exploiting those sources to simulate the noise propagation inside the duct due to the turbulent flow through the obstacle. In the two following sections, Curle's, Lighthill's and Ribner's analogies dealing with that acoustic wave propagation are presented and compared versus measurements.

2.6 DES Results

So as to be compared qualitatively to the experimental data, the results of the simulation are plotted in terms of velocity field (in m/s) near the constriction on a longitudinal slice located at $\boldsymbol{x = 92\ mm}$ and on transversal slices located at $\boldsymbol{z = -100\ mm}$ and $\boldsymbol{z = +30\ mm}$ from the center of the diaphragm (see Fig. 4). The values of the velocity field are averaged at each time step by OpenFOAM.

These results can be qualitatively compared to the experimental and numerical results of papers [15,17,21]. In the latter, a LES simulation has been performed on the same case. A very good agreement is observed with the experimental data. The DES predictions were unable to resolve the recirculation zones downstream the vena contracta but the averaged value calculated in those zones appears accurate enough not to affect the acoustic calculations (as will be seen in the following).

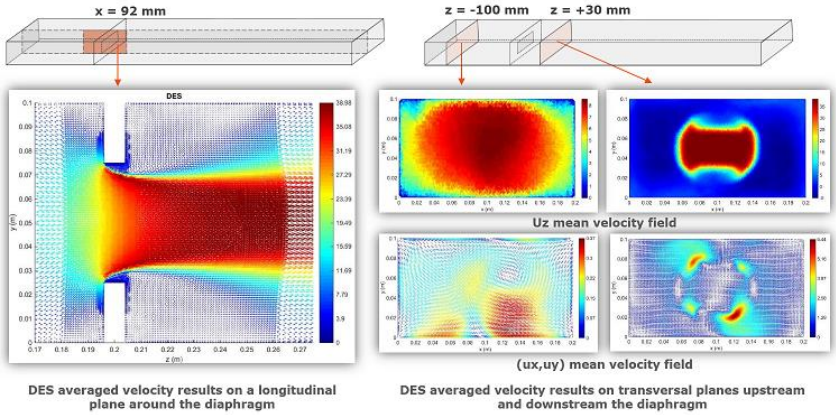

Figure 4. Visualization of the velocity field near the diaphragm on a slice at x = 92 mm (in m/s). The velocity field is not averaged on the entire DES time calculation.

At that stage, the equivalent aero-acoustic sources are computed thanks to the incompressible DDES CFD model described above and it is now a question of exploiting those sources to simulate the noise propagation inside the duct due to the turbulent flow through the obstacle. In the two following sections, Curle's, Lighthill's and Ribner's analogies dealing with that acoustic wave propagation are presented and compared.

3. BOUNDARY INTEGRAL FORMULATION OF CURLE'S ANALOGY

We consider the acoustic domain $\boldsymbol{V_{CFD}}$ as depicted in Fig. 5 with an obstacle inside a duct similar to the case presented for the CFD part above. The surfaces of the duct are rigid ($\boldsymbol{\Gamma_c}$) except the inlet $\boldsymbol{\Gamma_-}$ and the outlet $\boldsymbol{\Gamma_+}$ surfaces where an anechoic boundary condition is considered to simulate an infinite guide. The unit normal on the surface is oriented inside of the computational domain $\boldsymbol{V_{CFD}}$.

Figure 5. Computational domains (CFD and acoustic) and boundary conditions

The inhomogeneous wave propagation equation verified by the total pressure fluctuation $\widehat{\boldsymbol{P}}$ is considered in the Fourier domain, which takes the form of the Helmholtz equation:

$$\Delta\widehat{\boldsymbol{P}} + \boldsymbol{k^2}\widehat{\boldsymbol{P}} = \widehat{\boldsymbol{q}} \qquad \boldsymbol{in\ V_{CFD}} \tag{1}$$

In Equation 1, $\boldsymbol{k = \omega/c_0}$ and $\widehat{\boldsymbol{q}} = \boldsymbol{-\partial^2 T_{ij}/\partial x_i \partial x_j}$ with $\boldsymbol{T_{ij} = \widehat{T}_{ij} e^{i\omega t}}$ is Lighthill's tensor composed of a first term which is the fluctuations of speed $\boldsymbol{\rho u_i u_j}$, a second term $\boldsymbol{(p' - c_0^2 \rho')\delta_{ij}}$ similar to a fluctuation of entropy and a third term $\boldsymbol{\tau_{ij}}$ coming from the dissipation of energy by viscosity. We are interested in high Reynolds number with isentropic fluctuation of the pressure ($\boldsymbol{p - p_0 = c_0^2(\rho - \rho_0)}$) and low mach number flows ($\boldsymbol{(\rho - \rho_0) \propto M^2}$ i.e. $\boldsymbol{M < 0.3}$). With all of those hypotheses, The Lighthill's tensor becomes:

$$\boldsymbol{T_{ij} = \rho_0 u_i u_j} \tag{2}$$

corresponding to the turbulent velocity fluctuations. As the flow is incompressible at low Mach number, we can consider the total pressure

$$\widehat{\boldsymbol{P}} = \widehat{\boldsymbol{P}}_{\boldsymbol{a}} + \widehat{\boldsymbol{P}}_{\boldsymbol{h}} \tag{4}$$

with $\widehat{\boldsymbol{P}}_{\boldsymbol{a}}$ the acoustic and $\widehat{\boldsymbol{P}}_{\boldsymbol{h}}$ the hydrodynamic pressures and with $\widehat{\boldsymbol{P}}_{\boldsymbol{h}}$ the static solution ($\boldsymbol{k = 0}$) of Equation 1 given by

$$\Delta\widehat{\boldsymbol{P}}_{\boldsymbol{h}} = \widehat{\boldsymbol{q}} \qquad \boldsymbol{in\ V_{CFD}} \tag{5}$$

which can be written as its integral form:

$$\boldsymbol{C(x)}\widehat{\boldsymbol{P}}_{\boldsymbol{h}}\boldsymbol{(x,\omega)} = -\iiint_{\boldsymbol{V_{CFD}}} \widehat{\boldsymbol{G_0}} \frac{\boldsymbol{\partial^2 \widehat{T}_{ij}}}{\boldsymbol{\partial y_i \partial y_j}} \boldsymbol{dV} + \iint_{\boldsymbol{\partial V}} \left(\widehat{\boldsymbol{P}}_{\boldsymbol{h}} \frac{\boldsymbol{\partial \widehat{G_0}}}{\boldsymbol{\partial y_i}} \boldsymbol{.n_i} - \widehat{\boldsymbol{G_0}} \frac{\boldsymbol{\partial \widehat{P}_h}}{\boldsymbol{\partial y_i}} \boldsymbol{.n_i}\right) \boldsymbol{dS} \tag{6}$$

where $\widehat{\boldsymbol{G_0}}$ is the static Green's function. After subtracting Equation 6 to Equation 3,

$$C(x)\hat{P}_a(x,\omega) = -\iiint_{V_{CFD}} (\hat{G} - \widehat{G_0}) \frac{\partial^2 \hat{T}_{ij}}{\partial y_i \partial y_j} dV + \iint_{\partial V} \left(\hat{P} \frac{\partial \hat{G}}{\partial y_i} . n_i - \hat{G} \frac{\partial \hat{P}}{\partial y_i} . n_i \right) dS$$
$$- \iint_{\partial V} (\hat{P}_h \frac{\partial \widehat{G_0}}{\partial y_i} . n_i - \widehat{G_0} \frac{\partial \hat{P}_h}{\partial y_i} . n_i) dS \quad (7)$$

In Equation 6, the first volumetric integral in the right-hand-side is well-known [22] to not be numerically stable because of the second order of the derivation of the Lighthill's tensor. We solve this problem by using the Green's theorem twice. Furthermore, the surfaces ∂V of the domain V_{CFD} are divided into the rigid surfaces Γ_c and non-rigid surfaces $\Gamma_{\pm}$. By applying the boundary condition, the normal derivative of the pressure $\frac{\partial \hat{P}}{\partial y_i} . n_i{}_{|\Gamma_c} = 0$ as it is also the case for the velocity of the flow $u_{i_{|\Gamma_c}} = 0$, it leads to the following form

$$C(x)\hat{P}_a(x,\omega) = -\iiint_{V_{CFD}} \hat{T}_{ij} \frac{\partial^2 (\hat{G} - \widehat{G_0})}{\partial y_i \partial y_j} dV + \iint_{\Gamma_c} \hat{P}_a \frac{\partial \hat{G}}{\partial y_i} . n_i dS + \iint_{\Gamma_c} \hat{P}_h \frac{\partial (\hat{G} - \widehat{G_0})}{\partial y_i} . n_i dS$$
$$+ \iint_{\Gamma_{\pm}} \left(\hat{P}_a \frac{\partial \hat{G}}{\partial y_i} . n_i - \hat{G} \frac{\partial \hat{P}_a}{\partial y_i} . n_i \right) dS + \iint_{\Gamma_{\pm}} \left(\hat{P}_h \frac{\partial (\hat{G} - \widehat{G_0})}{\partial y_i} . n_i - (\hat{G} - \widehat{G_0}) \frac{\partial \hat{P}_h}{\partial y_i} . n_i \right) dS \quad (8)$$

This implicit integral formulation is a generalization of the Curle's analogy taking into account some non-rigid surfaces in the model and can be classically resolved using a BEM solver. This formulation for aero-acoustic simulation has been implemented inside the Boundary Element solver in the Vibro-Acoustic VAOne software. In general, to save some disk storage and CPU time and also because the volumetric quadrupole source term seems to be negligible for low frequency range, the first integral in the right-hand-side in Equation 8 is not computed. This Curle's analogy relies only on the Fluctuating Surface Pressure defined as the hydrodynamic pressure on the surfaces of the domain of computation. Nevertheless, if the Lighthill's tensor would be computed and stored during the CFD run, this volumetric source integral could be computed but would necessitate to discretize the volume V_{CFD} of the domain and evaluate the interaction between every element of the volumetric mesh with every element of the surface mesh.

4. FINITE ELEMENT FORMULATION OF LIGHTHILL AND RIBNER'S ANALOGIES

The theory behind the hybrid technique used in this part has been extensively described in several documents [2], [24]. The original idea of implementing a Lighthill's analogy in a Finite Element Method has been originally proposed by Oberai et al. [25], [26] and Ribner [29]. It is shortly summarized below. In the frequency domain, the standard FEM variational formulation of Lighthill's analogy in Equation 1 is:

$$\int_{V_{CFD}} \nabla \hat{P} \, \nabla v \, dV - k^2 \int_{V_{CFD}} \hat{P} \, v \, dV - ik\beta \int_{\Gamma_- \cup \Gamma_+} \hat{P} v \, dS$$
$$= -\int_{V_{CFD}} \frac{\partial \widehat{T_{ij}}}{\partial x_j} \frac{\partial v}{\partial x_i} dV + \int_{\Gamma_- \cup \Gamma_+} \frac{\partial \widehat{T_{ij}}}{\partial x_j} n_i v \, dS \quad (9)$$

where V_{CFD} is the computational volume of the duct and v is the test function used in the finite elements. The only unknown quantity in Equation 9 is the source term, represented by the divergence of Lighthill's tensor in the frequency domain. This quantity is computed by OpenFOAM using the density and velocity fields computed during the CFD run. This quantity is first computed in the time domain and a Fourier transform will then be used. The computation of the source term is performed using an updated version of OpenFOAM which calculates on the

CFD mesh the quantity $\frac{\partial \widehat{T_{ij}}}{\partial x_j} = \boldsymbol{Div}(\boldsymbol{\rho_0 u_i u_j})$ at the current time step used in Equation 9 after Fast Fourier Transfom. In this formulation, the source term is represented explicitly by the Lighthill's tensor given by Equation 2. Consequently, during the CFD computation, it is necessary to store the velocity field (real volume vector field) on the CFD mesh which is very expensive in term of disk storage. For industrial application, the number of vertices can easily reach several tens of millions which require several hundreds of Megabytes of storage for every time step. As an example, for a $\mathbf{20}$ Million cells CFD mesh, it is necessary to store $\mathbf{4 \times 3 \times 20 \,.\, 10^6 = 240\ Megabytes}$ for every time step. It is necessary to store the $\mathbf{3}$ components of the velocity volume vector field and $\mathbf{4}$ octets are necessary to store a real value in single precision for each component. For standard application, the number of time steps is several $\mathbf{1000}$ which leads finally to store hundreds of Gigabytes or even Terabytes.

Another approach enables to considerately reduce the CPU time and the disk storage working only with the pressure volume scalar field storing this quantity directly on the acoustic mesh. By subtracting Equation 5 to Equation 1 and using the definition of the total pressure in Equation 4**,** we obtain the following equation verified by $\widehat{\boldsymbol{P}}_{\boldsymbol{a}}$:

$$\begin{cases} \left(\boldsymbol{\Delta} + \boldsymbol{k^2}\right)\widehat{\boldsymbol{P}}_{\boldsymbol{a}}(\boldsymbol{x}) = -\boldsymbol{k^2}\widehat{\boldsymbol{P}}_{\boldsymbol{h}}(\boldsymbol{x}) \quad \boldsymbol{in\ V_{CFD}} \\ \boldsymbol{\partial_n}\widehat{\boldsymbol{P}}_{\boldsymbol{a}}(\boldsymbol{x}) + \boldsymbol{ik\beta}\widehat{\boldsymbol{P}}_{\boldsymbol{a}}(\boldsymbol{x}) = -\left(\boldsymbol{\partial_n}\widehat{\boldsymbol{P}}_{\boldsymbol{h}}(\boldsymbol{x}) + \boldsymbol{ik\beta}\widehat{\boldsymbol{P}}_{\boldsymbol{h}}(\boldsymbol{x})\right) = \boldsymbol{\gamma}(\boldsymbol{x}) \quad \boldsymbol{on\ \Gamma_- \cup \Gamma_+} \\ \boldsymbol{\partial_n}\widehat{\boldsymbol{P}}_{\boldsymbol{a}}(\boldsymbol{x}) = \boldsymbol{0} \quad \boldsymbol{on\ \Gamma_c} \end{cases} \tag{10}$$

which leads to the second FEM variational formulation of Lighthill's analogy:

$$-\int_{V_{CFD}} \frac{\mathbf{1}}{\boldsymbol{\rho}}\left(\boldsymbol{\nabla}\widehat{\boldsymbol{P}}_{\boldsymbol{a}}\boldsymbol{\nabla v}\right)\boldsymbol{dV} + \boldsymbol{\omega^2}\int_{V_{CFD}} \frac{\mathbf{1}}{\boldsymbol{\rho c^2}}\widehat{\boldsymbol{P}}_{\boldsymbol{a}}\boldsymbol{v}\,\boldsymbol{dV} + \boldsymbol{i\omega}\int_{\Gamma_- \cup \Gamma_+} \frac{\boldsymbol{\beta}}{\boldsymbol{\rho c}}\widehat{\boldsymbol{P}}_{\boldsymbol{a}}\boldsymbol{v}\,\boldsymbol{dS} =$$

$$-\boldsymbol{\omega^2}\int_{V_{CFD}} \frac{\mathbf{1}}{\boldsymbol{\rho c^2}}\widehat{\boldsymbol{P}}_{\boldsymbol{h}}\boldsymbol{v}\,\boldsymbol{dV} + \int_{\Gamma_- \cup \Gamma_+} \boldsymbol{\gamma v}\,\boldsymbol{dS} \tag{11}$$

where the source term is represented by the 3D hydrodynamic pressure field (real volume scalar field) only as distributed point sources in the volume. Compared to the previous formulation relying on the Lighthill's tensor as aero-acoustic sources in Equation 9, the size of the disk storage is divided by $\mathbf{3}$ which is already very interesting. Secondly, the mapping step between the sources CFD mesh and the acoustic target mesh is more straightforward, involving only scalar data at the center of the element instead of the three components of the velocity defined at the vertices of the CFD mesh. We describe more in details in the next part the source mapping algorithm.

5. SOURCE MAPPING AND INTERFACE WITH OPENFOAM

On one side, the initial source term in Equation 10, real volume scalar pressure field over the domain $\boldsymbol{V_{CFD}}$, is computed by the OpenFOAM solver for every time step on the CFD mesh. For industrial applications, even using hybrid DDES approach, this CFD mesh contains several millions of cells to be able to simulate all the complexity of the turbulence phenomena in details which is the noise generator. That CFD mesh will be called the source mesh in the following. On the other side, the acoustic mesh has to be generated to be able to simulate properly the acoustic propagation of the waves in the computational domain. The size of the acoustic mesh is fixed as a ratio of the acoustic wavelength. For the first order FEM element, for example, it is usually fixed for this application at $\boldsymbol{h = \lambda/10}$. Other mesh sizes are also tested at $\boldsymbol{h = \lambda/20}$ and at $\boldsymbol{h =}$

$\boldsymbol{\lambda/30}$ to measure the quality of the field transfer from the CFD to the acoustic meshes. That acoustic mesh will be called the target mesh in the following.

In general, for fields with polynomial representation on each cell, the components of the discretized field $\boldsymbol{\phi_s}$ on the source side can be expressed as linear combinations of the components of the discretized field $\boldsymbol{\phi_t}$ on the target side, in terms of a matrix-vector product:

$$\boldsymbol{\phi_t = W\phi_s} \tag{12}$$

where $\boldsymbol{W}$ is called the interpolation matrix. The objective of interpolators is to compute the matrix $\boldsymbol{W}$ depending on their physical properties and their mesh discretization. At the basis of many CFD numerical schemes is the fact that physical quantities such as density, momentum per unit volume or energy per unit volume obey some balance laws that should be preserved at the discrete level on every cell. It is therefore desired in aero-acoustic application that the process interpolation preserves the integral of $\boldsymbol{\phi}$ on any domain. At the discrete level, for any target cell $\boldsymbol{T_i}$, the following general interpolation formula has to be satisfied:

$$\iiint_{\boldsymbol{T_i}} \boldsymbol{\phi_t} = \sum_{\boldsymbol{S_j \cap T_i \neq \emptyset}} \iiint_{\boldsymbol{S_j \cap T_i}} \boldsymbol{\phi_s} \tag{13}$$

This equation is used to compute $\boldsymbol{W_{ij}}$, based on the fields representation of the real volume scalar pressure field and the geometry of source and target mesh cells. Another important property of the interpolation process is the maximum principle: the field values resulting from the interpolation should remain between the upper and lower bounds of the original field. When interpolation is performed between a source mesh $\boldsymbol{S}$ and a target mesh $\boldsymbol{T}$ the aspect of overlapping is important. In fact, if any cell of of $\boldsymbol{S}$ is fully overlapped by cells of $\boldsymbol{T}$ and inversely any cell of $\boldsymbol{T}$ is fully overlapped by cells of $\boldsymbol{S}$ that is

$$\sum_{\boldsymbol{S_j}} \boldsymbol{Vol}(\boldsymbol{T_i} \cap \boldsymbol{S_j}) = \boldsymbol{Vol}(\boldsymbol{T_i}) \quad \text{and} \quad \sum_{\boldsymbol{T_i}} \boldsymbol{Vol}(\boldsymbol{S_j} \cap \boldsymbol{T_i}) = \boldsymbol{Vol}(\boldsymbol{S_j}) \tag{14}$$

then the meshes $\boldsymbol{S}$ and $\boldsymbol{T}$ are said to be overlapping. In this case the two formulas in a given column in the table below give the same result. All intensive formulas result in the same output, and all the extensive formulas give also the same output. The ideal interpolation algorithm should be conservative and respect the maximum principle. However, such an algorithm can be impossible to design if the two meshes do not overlap. When the meshes do not overlap, using either $\boldsymbol{Vol}(\boldsymbol{T_i})$ or $\boldsymbol{Vol}(\boldsymbol{T_i} \cap \boldsymbol{S_j})$ one obtains an algorithm that respects either the conservation or the maximum principle.

For intensive fields such as it is the case for the pressure or the Lighthill's tensor for our application, the left hand side in Equation 13 in the general interpolation equation becomes:

$$\iiint_{\boldsymbol{T_i}} \boldsymbol{\phi} = \boldsymbol{Vol}(\boldsymbol{T_i})\boldsymbol{\phi_{T_i}} \tag{15}$$

In the general interpolation equation, the right hand side in Equation 13 becomes:

$$\sum_{\boldsymbol{S_j \cap T_i \neq \emptyset}} \iiint_{\boldsymbol{S_j \cap T_i}} \boldsymbol{\phi} = \sum_{\boldsymbol{S_j \cap T_i \neq \emptyset}} \boldsymbol{Vol}(\boldsymbol{S_j} \cap \boldsymbol{T_i})\boldsymbol{\phi_{S_j}} \tag{16}$$

As the field values are constant on each cell, the coefficients of the linear remapping matrix $\boldsymbol{W}$ are given by the formula:

$$\boldsymbol{W_{ij}} = \frac{\boldsymbol{Vol}(\boldsymbol{S_j} \cap \boldsymbol{T_i})}{\boldsymbol{Vol}(\boldsymbol{T_i})} \tag{17}$$

The very hard technical point of this method consists in computing the intersected volume (numerator in the fraction in Equation 17) between one element of the source mesh and one element of the target mesh. This development has been realized inside the OpenFOAM+ v3.0 by the OpenCFD team. The mapping can be done on the fly during the CFD computation at the end of every converged time step before storing the hydrodynamic pressure or the Lighthill's tensor or in a post processing stage at the end of the CFD computation. This choice depends essentially on the disk storage capabilities and also if the target acoustic mesh is susceptible to change during the study.

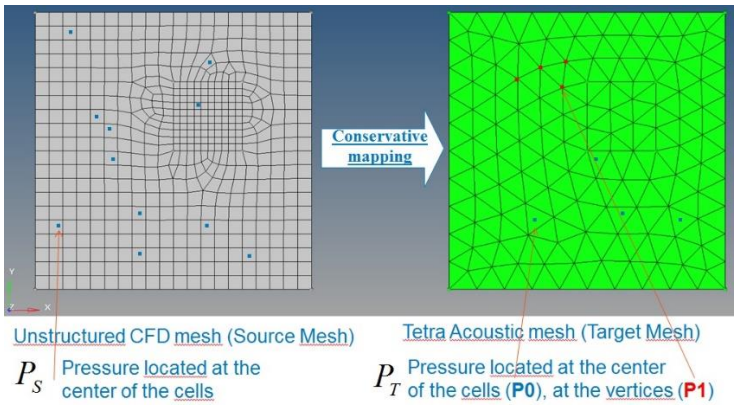

Figure 6. Conservative mapping concept

For aero-acoustic application using FEM approach, in practice, the process is the following:

- Run the CFD OpenFOAM DES solver. During the CFD computation, the real volume scalar pressure field or the vector $\frac{\partial \widehat{T_{ij}}}{\partial x_j}$ field are mapped from the CFD mesh to the acoustic mesh on the fly and then exported in the Ensight format.
- Perform a Fourier Transform with Han's window with overlapping over segments if the signal is long enough.
- Run the FEM aero-acoustic solver using the aero-acoustic sources previously computed to evaluate the generated noise modelled by the Lighthill's or Ribner formulations.

By proceeding this way, the disk storage and the CPU time are minimal keeping a very good accuracy as it will be presented in the last part on the validation case. This process has the advantage that the CFD and the CAA are completely decorrelated. They can be done by different persons who don't interact directly. This method appears like the best approach for industrial application. Indeed, it removes the only drawback: the quite large amount of data to be stored on disks by doing the mapping on the fly and enables to take into account all the aero-acoustic sources in the computational domain and not only the Fluctuating Surface Pressure in the BEM approach. If several acoustic meshes are planned to be used, it is also possible to store the aerodynamic pressure or $\frac{\partial \widehat{T_{ij}}}{\partial x_j}$ during the CFD computation on the CFD mesh and do the conservative mapping after all. But this solution imposes a very large disk storage for big industrial application cases. As illustrated on Figure 7, the $\frac{\partial \widehat{T_{ij}}}{\partial x_j}$ is mapped from the CFD fine mesh to different acoustic coarse meses ($\lambda/10$, $\lambda/20$ and $\lambda/30$ for P1 tetrahedron TE4 elements and $\lambda/10$ for P2 tetrahedron TE10 elements).

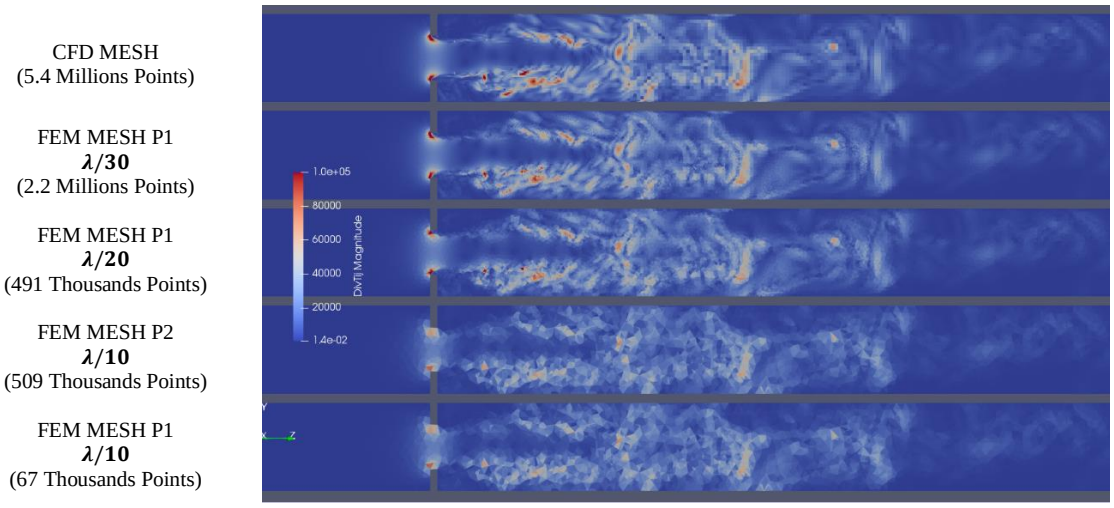

Figure 7. $\frac{\partial \widehat{T_{ij}}}{\partial x_j}$ Volume Vector Field (magnitude) on the CFD mesh and mapped on different FEM meshes.

Despite the detailed representation of the different source zones seems to be different comparing those different contour plots of the $\frac{\partial \widehat{T_{ij}}}{\partial x_j}$, as it has been explained the conservative mapping ensures the integral of the quantity is conserved over the meshes so the quality results should be independant of the mesh size.

In future work, the source zone will be defined by localizing the high levels of Turbulent Kinetic Energy Dissipation ($\boldsymbol{\varepsilon}$) delivered by a first RANS simulation as illustrated in Fig. 8 which corresponds to high level of hydrodynamic pressure $\widehat{\boldsymbol{P_h}}$ or the simple divergence of the Lighthill's tensor $\frac{\partial \widehat{T_{ij}}}{\partial x_j}$. The Turbulent Kinetic Energy Dissipation ($\boldsymbol{\varepsilon}$) can be also linked to the frequency cut-off by

$$\boldsymbol{F_{cut-off} = \alpha \times \varepsilon^{1/3} \times \Delta_x^{-2/3}} \tag{18}$$

where $\boldsymbol{\alpha}$ is constant to be defined ($\boldsymbol{\alpha = 1}$), $\boldsymbol{\Delta_x}$, the local element size of the CFD mesh ($\boldsymbol{m}$) and finally $\boldsymbol{\varepsilon}$ the turbulent dissipation rate ($\boldsymbol{m^2/s^3}$).

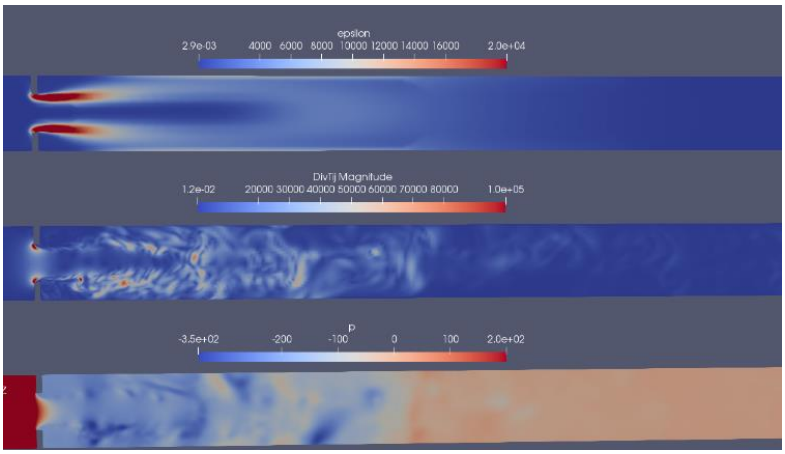

Figure 8. Turbulent Kinetic Energy ($\boldsymbol{\varepsilon}$), Hydrodynamic pressure $\widehat{\boldsymbol{P_h}}$ or the simple divergence of the Lighthill's tensor $\frac{\partial \widehat{T_{ij}}}{\partial x_j}$ on the CFD mesh to define source zone for the acoustic simulation.

5. APPLICATION CASE

The CFD results of the DDES achieved in this paper are used as an input data of both previously presented acoustic analogies (FEM and BEM). A visualization of the interpolated hydrodynamic pressure field obtained by DES is presented in Fig. 9. One can observe the fluctuation zone right downstream the diaphragm.

For the FEM Lighthill's and Ribner's analogies, the mesh size fixed at $\boldsymbol{\lambda/10}$ leads to $\mathbf{67\,836}$ nodes, at $\boldsymbol{\lambda/20}$ leads to $\mathbf{491\,848}$ nodes, at $\boldsymbol{\lambda/30}$ leads to $\mathbf{2\,202\,370}$ nodes for P1 TE4 element and finally at $\boldsymbol{\lambda/10}$ leads to $\mathbf{509\,264}$ nodes for P2 TE10 elements. The hydrodynamic time pressure data $\boldsymbol{P_h}$ and the simple divergence of the Lighthill's Tensor $\frac{\partial \widehat{T_{ij}}}{\partial x_j}$, (volumetric quantities) just needs to be FFT. Indeed, the volumetric conservative mapping step is done on the fly during the CFD computation.

For both acoustic BEM and FEM computations, the inlet and outlet faces are set to a non-reflective boundary condition to avoid diffraction issues at both sides of the duct. The acoustics calculation is performed on the frequency range $[\mathbf{200-3500}]$ $\boldsymbol{Hz}$ by frequency steps of $\mathbf{20}$ $\boldsymbol{Hz}$ ($\mathbf{166}$ frequencies). A sensor, recording acoustic pressure on the wall inside the duct, is placed far upstream the diaphragm (see Fig. 9) at a point located at $(\boldsymbol{x,y,z}) = (\mathbf{0,0.0386,1.285})$ $\boldsymbol{m}$.

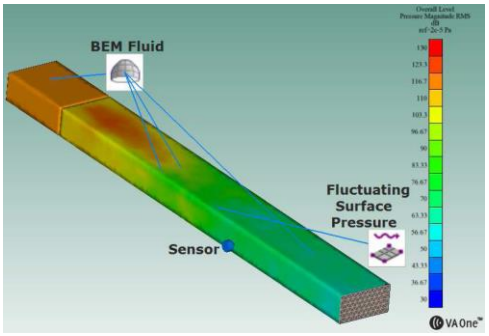

Figure 9. Set-up of the acoustics BEM case on VA One and visualization of the interpolated DES CFD frequency data on the diaphragm mesh (overall level on frequencies 200 to 3500 Hz).

Fig 10 shows the results of the measured and computed Sound Pressure Levels (SPL) at this latter point with both numerical FEM methods with only a single time interval. The experimental result obtained on UTC's bench test is plotted in black full line. The cut-off frequencies of that duct ($\mathbf{0.2m \times 0.1m}$ rectangular section) are plotted by the magenta dashed lines.

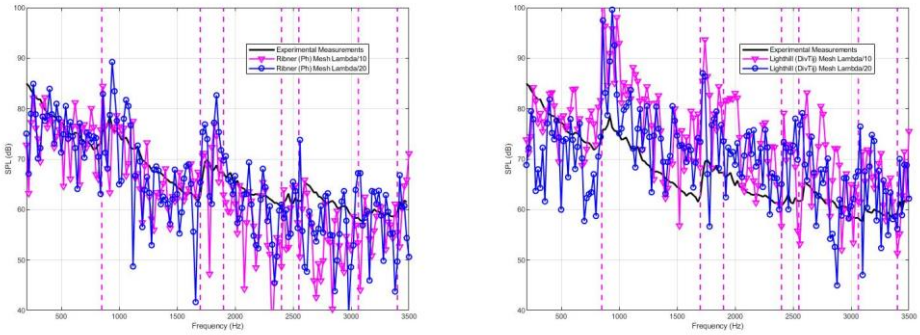

Figure 10. Comparison of experimental and numerical SPL obtained with Ribner's (left) and Lighthill's (right) FEM analogies with two acoustic mesh sizes.

One can observe that the SPL results issued from DES chaining with both FEM methods are in very good agreement for all the frequency range (except jumps at cut-off frequencies) with the experimental SPL. For BEM results on the same results, one can refer to [15]. It can be seen the quality of the results are almost indepandant of the FEM formulations and the mesh size which demonstrates the quality of the computation of simple divergence of the Lighthill's tensor $\frac{\partial \widehat{T_{ij}}}{\partial x_j}$ on the CFD mesh and the efficiency of the 3D volume conservative mapping in OpenFOAM to transfer equivalenet aero-acoustic sources from one mesh to another one. The last point is the experimental curve is less fluctuating compared with numerical results because the measurements are averaged over 256 segments whereas numerical ones are not averaged yet. In the presentation, signal average will be performed to reduce the fluctuations by increasing the CFD simulated physical duration to consider several time intervals (10 or more) with overlapping (50%).

5. CONCLUSION

An approach combining the 3D volumetric Finite Element Method with Lighthill's and Ribner analogies aero-acoustic sources and the CFD open source OpenFOAM solver has been implemented. It has been applied to a benchmark for computational aero-acoustic: the sound produced by a 3D ducted diaphragm. For the CFD point of view, the DDES enables to reduce considerably the CPU time keeping good enough precision to compute the equivalent aero-acoustic sources. For the acoustic one, the results obtained by the FEM solvers is in a very good agreement with experimental measurements for all the frequency range $[\mathbf{200}:\mathbf{3500}]\boldsymbol{Hz}$. Thanks to a conservative mapping on the fly between the CFD and the acoustic meshes, the disk storage is also minimized (not exceeding few Gbs) and enables to simulate very complex 3D industrial applications. During the presentation, other solutions to reduce the CPU time/disk storage will be demonstrated (limited source zone for example) and averaging with several time signals to reduce result fluctuations. This 3D volumetric Finite Element Method with Lighthill's analogy formulation will be extended to a porous formulation to consider low speed Fan Noise. Some validation cases will be shown in the very near future to demonstrate its capabilities in another coming paper.

5. ACKNOWLEDGEMENTS

This work is part of the CEVAS (Conception d'Equipement de Ventilation d'Air Silencieux) project, funded by Région Picardie and FEDER.

6. REFERENCES

[1] Crighton, D. G. Computational aeroacoustics for low Mach number flows, Computational Acoustics, J. C. Hardin, M. Y. Hussaini (Eds.), Springer, New York, (1992), 50–68.
[2] Lighthill, M. J. On sound generated aerodynamically: I. General theory, Proceedings of the Royal Society A, 221, 564–587, (1952).
[3] Curle, N. The influence of solid boundaries upon aerodynamic sound, Proceedings of the Royal Society A, 231, 505–514, (1955).
[4] Ffowcs Williams, J. E., Hawkings, D. L. Sound generated by turbulence and surfaces in arbitrary motion, Philosophical Transactions of the Royal Society A, 264, 321–342, (1969).
[5] Ryu, J., Cheong, C., Kim, S., Lee, S. Computation of internal aerodynamic noise from a quick opening throttle valve using frequency-domain acoustic analogy, Applied Acoustics, 66, 1278 1308, (2005).
[6] Yasuda, T., Wua, Ch., Nakagawa, N., Nagamura, K. Predictions and experimental studies of the tail pipe noise ofan automotive muffler using a one dimensional CFD model, Applied Acoustics, 71, 701–707, (2010).
[7] Davies, H. G., Ffowcs Williams, J. E. Aerodynamic sound generation in a pipe, Journal of Fluid Mechanics, 32, 765–778, (1968).

[8] Nelson, P. A., Morfey, C. L. Aerodynamic sound production in low speed ducts, Journal of Sound and Vibration, 79, 263–289, (1981).
[9] Peters, M. C. A. M., Hirschberg, A. Acoustically induced periodic vortex shedding at sharpedged open channel ends: Simple vortex models, Journal of Sound and Vibration, 161, 281–299, (1993).
[10] Piellard, M., Bailly, C. Several computational aeroacoustics solutions for the ducted diaphragm at low Mach number, 16th AIAA/CEAS Aeroacoustic Conference, AIAA paper 2010–3996, (2010).
[11] Venkatesham, B., Tiwari, M., Munjal, M. L. Prediction of breakout noise from a rectangular duct with compliant walls, International Journal of Acoustics and Vibration, 16 (4), 180–190, (2011).
[12] Mak, C. M. A prediction method for aerodynamic sound produced by multiple elements in air ducts, Journal of Sound and Vibration, 287, 395–403, (2005).
[13] Han, N., Mak, C. M. Prediction of flow-generated noise produced by acoustic and aerodynamic interactions of multiple in-duct elements, Applied Acoustics, 69, 566–573, (2008).
[14] Bennouna, S., Naji, S., Cheriaux, O., Moreau, S. et al., "Aeroacoustic Prediction Methods of Automotive HVAC Noise," SAE Technical Paper 2015-01-2249, 2015, doi:10.4271/2015-01-2249.
[15] Escouflaire, M., Zerbib, N., Mas, D., Papaxanthos, N. et al., "Numerical Aeroacoustics Prediction of a Ducted Diaphragm Chaining RANS-LES and DES Results to a Parallel Boundary Element Method," SAE Technical Paper 2016-01-1810, 2016, doi:10.4271/2016-01-1810.
16 Schram, C. A boundary element extension of Curle's analogy for non-compact geometry at low Mach number, Journal of Sound and Vibration, 322, 264–281, (2009).
[17] Papaxanthos, N., Perrey-Debain Emmanuel, On the use of integral formulations for the prediction of air flow noise in ducts, ICSV22, Florence, Italy, (2015).
[18] Spalart, P. R. , Jou, W.H. , Strelets, M. and Allmaras, S.R., Comments on the Feasibility of LES for Wings, and on a Hybrid RANS/LES Approach. Advances in DNS/LES, 1st AFOSR Int. Conf. on DNS/LES, Greyden Press, Columbus, H., Aug. 4-8, 1997.
[19] Spalart, P.R., Deck, S., Shur, M. and Squires, K.D., A New Version of Detached-Eddy Simulation, Resistant to Ambiguous Grid Densities, Theoritical and Computational Fluid Dynamics, vol. 20, pp. 181–195, 2006.
[20] Menter, F.R. and Kuntz, M., Adaptation of Eddy-Viscosity Turbulence Models to Unsteady Separated Flow Behind Vehilces, The Aerodynamics of Heavy Vehicles: Trucks, Buses and Trains, Edited by McCallen, R. Browand, F. and Ross, J., Springer, Berlin Heidelberg New York, 2004, 2-6 Dec. 2002.
[21] Papaxanthos N., Perrey-Debain E., Ouedraogo B., Moreau S. et al., Prediction of Air Flow Noise in Ducts due to the Presence of Fixed Obstacles, Proceedings of Euronoise 2015, Maastricht, Netherlands, 2015
[22] Schram C., Martinez-Lera P., and Tournour M. Two-dimensional in-duct vortex leapfrogging as a validation benchmark for internal aeroacoustics. 13th AIAA/CEAS Aeroacoustics conference, AIAA 2007-3565, 2007.
[23] Watigrant, M., Picard, C., Perrey-Debain, E., Prax, C., Formulation adaptée de l'analogie acoustique de Lighthill-Curle en zone source, 19eme Congrès Français de Mécanique, Marseille, 24-28 Aout 2009.
[24] Caro, S., Ploumhans, P., and Gallez, X., _Implementation of Lighthill's Acoustic Analogy in a Finite/Infinite Elements Framework, AIAA Paper 2004-2891, 10th AIAA/CEAS Aeroacoustics Conference and Exhibit, 10-12 May 2004, Manchester, UK.
[25] Oberai, A. A., Roknaldin, F., Hughes, T. J. R. Computational procedures for determining structural-acoustic response due to hydrodynamic sources, Computer Methods in Applied Mechanics and Engineering, 190, 345–361, (2000).
[26] Oberai, A. A., Roknaldin, F., Hughes, T. J. R., Computation of Trailing-Edge Noise due to Turbulent Flow over an Airfoil, Vol. 40, pp. 2206-2216, 2002
[27] Howe, M. S., Theory of Vortex Sound, Cambridge Texts in Applied Mathematics, 2003.
[28] Caro, S., Sandboge, R., Iyer, J., Nishio, Y., Presentation of a CAA formulation based on Lightill's analogy for fan noise, Fan Noise Paper, 2007, Lyon, France.

[29] Ribner, H.S., The Generation of Sound by Turbulent Jets, Advances in Applied Mechanics, 1964, Volume 8, pages 103-182.